

# CrystEngComm

Accepted Manuscript



This is an *Accepted Manuscript*, which has been through the Royal Society of Chemistry peer review process and has been accepted for publication.

*Accepted Manuscripts* are published online shortly after acceptance, before technical editing, formatting and proof reading. Using this free service, authors can make their results available to the community, in citable form, before we publish the edited article. We will replace this *Accepted Manuscript* with the edited and formatted *Advance Article* as soon as it is available.

You can find more information about *Accepted Manuscripts* in the [Information for Authors](#).

Please note that technical editing may introduce minor changes to the text and/or graphics, which may alter content. The journal's standard [Terms & Conditions](#) and the [Ethical guidelines](#) still apply. In no event shall the Royal Society of Chemistry be held responsible for any errors or omissions in this *Accepted Manuscript* or any consequences arising from the use of any information it contains.

## ARTICLE

## Transition of crystallographic and electronic structures in In-Zn-Se alloys grown by molecular beam epitaxy

Cite this: DOI: 10.1039/x0xx00000x

Received 00th January 2012,  
Accepted 00th January 2012

DOI: 10.1039/x0xx00000x

[www.rsc.org/](http://www.rsc.org/)Ling Lee,<sup>a\*</sup> Liang-Kuei Huang,<sup>b</sup> Chu-Shou Yang,<sup>b\*</sup> Shang-Jui Chiu,<sup>c</sup> Chia-Hsin Wang,<sup>c</sup> Jeng-Lung Chen,<sup>c</sup> Ching-Shun Ku,<sup>c</sup> Jyh-Fu Lee,<sup>c</sup> and Hsin-Yi Lee<sup>c</sup>

In this work, we demonstrated the dependence of crystallographic characteristics and electronic structures on indium amounts in the indium-zinc-selenium alloy fabricated by vapour-phase deposition. By taking advantages of the molecular beam epitaxy and synchrotron radiation apparatus, it is shown for the first time that the significant difference of vapour pressure between zinc and indium induced deficient zinc in solid state, and resulted in a transition of five distinguished phases in the whole range of the alloy from zinc selenide to indium selenide. The binary ZnSe with indium dopants, the ZnSe-rich alloy with a minority of ZnIn<sub>2</sub>Se<sub>4</sub>, the disordered structure owing to the comparable mixture of ZnSe and ZnIn<sub>2</sub>Se<sub>4</sub>, the ZnIn<sub>2</sub>Se<sub>4</sub>-rich alloy with a minority of ZnSe, and the binary In<sub>2</sub>Se<sub>3</sub> phase are separated by the indium incorporation ratio of 0.01, 0.02, 0.18, and 0.69, respectively. Moreover, a pronounced carrier localisation effect was observed in the ZnSe-rich and disordered mixture. The wide-distributed mid-gap states were attributed to a high density of zinc vacancies in the ZnSe-based lattice. In brief, these fundamental properties would provide feasibilities of Se-based II-III<sub>2</sub>-VI<sub>4</sub> alloys for optoelectronics.

### Introduction

Ternary and quaternary selenide compounds continuously act as promising materials for optoelectronic applications. One of the most attractive selenide is the chalcopyrite CuIn<sub>1-x</sub>Ga<sub>x</sub>Se<sub>2</sub> (CIGS), which is capable for replacing Si-based photovoltaic devices. Solar cells with a conversion efficiency of 20.3% had been achieved based on the CIGS absorbing layer<sup>1</sup>. Besides the quaternary alloy, II-III<sub>2</sub>-Se<sub>4</sub> ternary alloys gained considerable interests. Because of the high photosensitivity in the visible range, cadmium indium selenide (CdGa<sub>2</sub>Se<sub>4</sub>) encouraged potential applications on photodetection and radiation measurements<sup>2</sup>. Cadmium indium selenide (CdIn<sub>2</sub>Se<sub>4</sub>) with a narrower bandgap make it an alternative candidate for photovoltaic application<sup>3</sup>. As for ZnIn<sub>2</sub>Se<sub>4</sub>, various feasibilities had been reported, including the photoelectrochemical cells<sup>4</sup>, the absorbing layer of solar cells<sup>5</sup>, and the buffer layer<sup>6</sup> between the p-type CIGS absorbing layer and the n-type ZnO window layer. However, although ZnIn<sub>2</sub>Se<sub>4</sub> satisfies various potential fields, some uncovered problems remain. In particular, incorporating a group-III element into the II-VI compound shows high probabilities to alter the crystalline ordering. Hence the exact stoichiometry for generating ordered ZnIn<sub>2</sub>Se<sub>4</sub> in the indium-zinc-selenium alloy would be a critical technique challenge. In addition, the optical properties for not only the

ZnIn<sub>2</sub>Se<sub>4</sub>, but also other phases in the In-Zn-Se alloy would be complicated and require comprehensive studies.

Recently, fabricating ZnIn<sub>2</sub>Se<sub>4</sub> compound had been attempted by using various processes such as spray pyrolysis<sup>5</sup>, coevaporation<sup>6</sup>, vertical bridgeman technique<sup>7</sup>, and the selenisation of Zn-In metal alloy<sup>4,8</sup>. Nevertheless, almost all of the results exhibit polycrystalline and non-stoichiometric nature. For instance, as for the In-Zn-Se alloy fabricated by the selenisation process of Zn-In metal alloy, one group found a dominant structure of polycrystalline ZnSe as the indium composition below 0.5<sup>8</sup>, whereas the other group found a polycrystalline ZnIn<sub>2</sub>Se<sub>4</sub> structure as the indium composition between 0.24 and 0.39<sup>4</sup>. Up to date, it is still lacking in the discovery of these uncertainties. Moreover, the electronic structure in the Zn-In-Se alloy exhibits similar uncertainties.

Previously, slightly indium doping with concentration of about 10 to 50 ppm had been performed for raising conductivity of ZnSe single crystals by several orders of magnitude<sup>9-11</sup>. However, once the indium content reaches 0.1 %, a large resistivity of 10<sup>5</sup> Ω-cm and a pronounced yellow emission were observed as interpreted by the self-compensating effect. As for the abovementioned polycrystalline ZnIn<sub>2</sub>Se<sub>4</sub>, a direct transition at room temperature of 1.68-1.81 eV was observed<sup>4</sup>. On the contrary, some results reveal a direct bandgap of 1.774 eV with an indirect bandgap of 1.624 eV<sup>7</sup>. For the sake of

overcoming these uncertainties, accurate investigations on both the crystalline characteristics and physical properties in the In-Zn-Se alloy as a function of solid solubility of indium are required.

In this article, In-Zn-Se alloys were grown by molecular beam epitaxy on GaAs(100) substrate, and the whole range of composition from zinc selenide to indium selenide was controlled by the vapour flux of each element. For the sake of precise characterizations, synchrotron radiation apparatus were performed. The crystallographic transition of the vapour-phase deposited In-Zn-Se alloy was demonstrated for the first time to accomplish the growth phase diagram of the alloy. Following investigations on the corresponding electronic structures and optical properties of the crystallographic transition were also revealed. The origin of the variable stoichiometry, crystallography, and electronic structure was discussed in this work, which would provide effective fundamental knowledge of this material.

### Experimental details

Thin films of In-Zn-Se alloys were grown on semi-insulating GaAs(100) substrates at 400 °C by using a home-made molecular beam epitaxy (MBE) system. For the purpose of a better crystalline quality, the reference binary ZnSe thin film was grown under a Se-rich condition. Under the same condition, In-Zn-Se alloys were grown as the effusion cell temperature of indium was varied from 350 to 650 °C. As for another reference, an InSe specimen was grown as the indium cell of 650 °C without zinc flow. The thickness of these specimens was extracted by scanning electron microscopy. In comparison to the binary ZnSe, the thickness decreases from 320 to 240 nm as the In cell temperature reaches 400 °C. A minimum thickness of 48 nm occurs at the temperature of 450 °C. Further increases of the indium supply result in the thickness between 120 and 150 nm. The stoichiometric properties of these alloys were measured by energy dispersion x-ray spectroscopy (EDX). The crystallographic investigations were performed by x-ray diffraction (XRD), in which x-ray beam were generated by an in-house Cu K<sub>α</sub> source ( $\lambda=1.540$  Å) and the wiggler synchrotron radiation beamline BL17B ( $\lambda=1.549$  Å) in National Synchrotron Radiation Research Center (NSRRC), Taiwan. As for the investigations on local atomic structures and defects, extended x-ray absorption fine structure (EXAFS) above the Zn K-edge (9,659 eV) was carried out at the wiggler synchrotron radiation beamline BL17C in NSRRC. Measurements were operated in fluorescence mode using a gas ionisation chamber with an energy resolution of about 1 eV. The EXAFS spectra were analysed using the standard procedure of software Athena 0.8.056, and Artemis 0.8.012 program with the IFEFFIT package. Furthermore, the electronic structures and the recombination processes of the thin films were investigated by the x-ray photoelectron spectroscopy (XPS), the reflectance, and the photoluminescence (PL) measurements. The XPS measurement was operated at a WR-SGM synchrotron beamline BL24A in

Table 1 Normalized atomic composition of In, Zn, and Se in the In-Zn-Se alloy and the reference specimens.

In cell temperature (°C)	[In]/([In]+[Zn]+[Se])	[Zn]/([In]+[Zn]+[Se])	[Se]/([In]+[Zn]+[Se])
0	0	0.460	0.540
350	0	0.427	0.573
400	0	0.406	0.594
450	0.007	0.336	0.657
500	0.012	0.358	0.630
600	0.069	0.319	0.612
630	0.093	0.208	0.699
640	0.116	0.240	0.644
650	0.202	0.091	0.707
650 *	0.281	0	0.719

\* without Zn flow

NSRRC in the condition of an exciting energy of 750 eV with an energy resolving power of 10,000. The reflectance and photoluminescence measurements were excited by a halogen lamp and a diode laser at 403 nm, respectively. The optical signals were analysed by a Horiba Jobin-Yvon iHR550 0.5-m monochromator and detected by an LN<sub>2</sub>-cooled charge-coupled device with an energy resolution of 0.3 meV.

### Results and discussion

#### 1. Transition of stoichiometry and crystallography

Table 1 shows the normalized atomic composition of indium, zinc, and selenium in the In-Zn-Se alloy and the reference specimens. The incorporation ratio of indium to all the cations, [In]/([In]+[Zn]), was introduced in this study as shown in Fig. 1. Under our growth condition, the ZnSe thin film exhibits a Se-rich condition with [Zn]/[Se]~0.85. A clear decreasing of [Zn]/[Se] to ~0.51 was found as the indium cell temperature at 450 °C in which the indium incorporation ratio is 0.02. When the indium cell temperature exceeds 600 °C, large amount of incorporated indium atoms was observed in solid

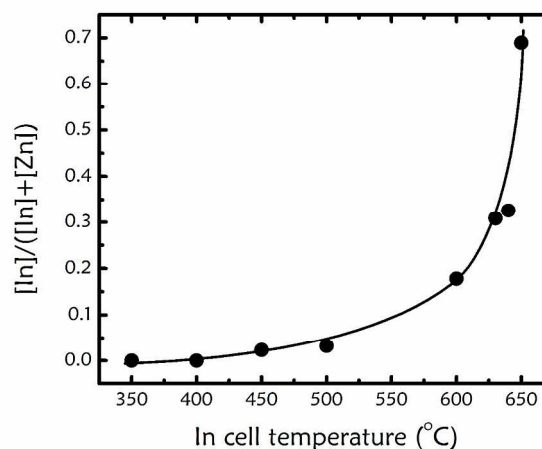


Fig. 1 The indium incorporation ratio in the Zn-In-Se alloy as the function of In cell temperature

state with a similar trend of selenium, whereas the relative composition of zinc is dramatically decreased. It implies that the indium incorporation hinders the solid composition of zinc. For instance, as the indium cell temperature reached 650 °C, a value of [Zn]/[Se] of ~0.13 was observed. To our knowledge, this significant drop of relative solid solubility of Zn during the vapour-phase deposition of Zn-In-Se alloy was not usually discussed. We proposed a reasonable interception based on the different vapour pressure of each element. At the substrate temperature of 400 °C during growth, the vapour pressure of zinc is about 0.1 mmHg, which is significantly larger than that of indium of less than 10<sup>-8</sup> mmHg<sup>12</sup>. Therefore, during a simultaneous supply of indium and zinc, the latter exhibits much more opportunities to escape from the surface before finishing the strong chemical bond and deficient zinc in the solid-state In-Zn-Se alloy is expected.

After justifying the atomic composition during vapour-phase deposition, crystallographic properties corresponding to various compositions in the In-Zn-Se alloy were demonstrated by using the x-ray diffraction. Figure 2(a) shows the radial ( $\theta$ - $2\theta$ ) scans along the surface normal by using in-house instruments. Pronounced diffractions from GaAs(200) and GaAs(400) were observed at  $2\theta$  of ~31.6° and ~66.0°, respectively. A broad hump at the high-angle side of GaAs(200) was considered as the diffracted signals by the Cu K $\beta$  line of the in-house x-ray source. Besides, some additional peaks from the

thin film appear in the diffraction spectra. As the indium cell temperature is less than 450 °C, in which the corresponding indium incorporation ratio is 0.02, a shoulder centred at  $2\theta$  of ~65.8° was observed and attributed to the diffraction peaks from ZnSe(400). The centre position of the shoulder seems insensitive to the indium amount, which indicates that the crystal structure under the low-level indium incorporation is dominated by the ZnSe phase. As the indium cell temperature increases from 450 to 600 °C, the indium incorporation ratio increases from 0.03 to 0.18 and the ZnSe(400) diffraction shoulder became weaker and more broadened. It implies a disordered phase occurred in the alloy. In addition, an apparent change in the alloy structure occurs once the indium cell temperature exceeds 630 °C. Within a 20 °C increment, it was found an increase of indium incorporation ratio from 0.30 to 0.69, together with three additional peaks in the XRD scans at  $2\theta$  of ~15.6°, ~47.5°, and ~65.0°. It indicates that new crystalline phases could be created under high-level indium incorporation. According to the Joint Committee on Powder Diffraction Standard database (JCPDS), the peak at ~65.0° could be attributed to the diffraction from the (008) plane of tetragonal ZnIn<sub>2</sub>Se<sub>4</sub> (JCPDS No.75-0741). However, the peak at ~15.6° is similar to the diffraction from either the ZnIn<sub>2</sub>Se<sub>4</sub>(002) at ~15.4° or the (101) plane of  $\gamma$ -In<sub>2</sub>Se<sub>3</sub> (JCPDS No.65-3639) at ~15.0°. The peak at ~47.5° also shows similar condition, in which ZnIn<sub>2</sub>Se<sub>4</sub>(006) and  $\gamma$ -In<sub>2</sub>Se<sub>3</sub>(208) reveals

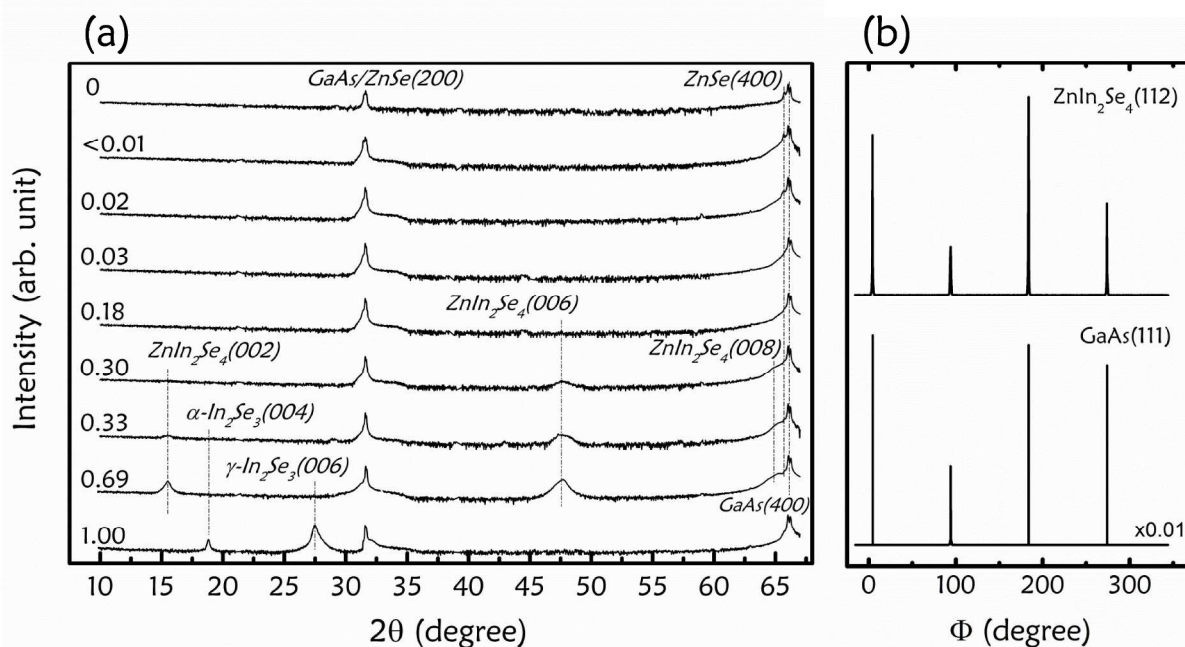


Fig. 2 (a) Surface-normal x-ray radial scan for In-Zn-Se with various indium incorporation ratio and the reference specimens. (b) Azimuthal scans of GaAs(111) and ZnIn<sub>2</sub>Se<sub>4</sub>(112).

diffraction near  $\sim 47.6^\circ$ . In order to identify the origins of the new generated peaks, off-normal XRD radial scans were also implemented. Diffractions from  $\text{ZnIn}_2\text{Se}_4$  which was reported in the database of JCPDS were apparent, while those from  $\gamma\text{-In}_2\text{Se}_3$  were not observed by either in-house or synchrotron radiation apparatus. Moreover, azimuthal scans as shown in Fig. 2(b) reveal four  $90^\circ$ -separated peaks from  $\text{ZnIn}_2\text{Se}_4(112)$  which verified the four-fold symmetry of the tetragonal structure. The azimuthal scan from GaAs(111) was also plotted in Fig. 2(b) and the in-plane epitaxial relationship between  $\text{ZnIn}_2\text{Se}_4$  and the substrate follows  $[110]_{\text{ZnIn}_2\text{Se}_4} // [110]_{\text{GaAs}}$ .

Furthermore, the effect of zinc incorporation on the crystalline properties in the indium-rich region of the In-Zn-Se alloy was also discussed. As shown in Fig. 2(a), the reference InSe specimen with  $[\text{In}]/[\text{Se}] \sim 0.39$  exhibits diffraction peaks at  $\sim 18.5^\circ$ , and  $\sim 27.8^\circ$ . The former is considered as the diffraction from the (004) plane of  $\alpha\text{-In}_2\text{Se}_3$  (JCPDS No.34-1279). The latter could be attributed to  $\alpha\text{-In}_2\text{Se}_3(006)$  as well as the  $\gamma\text{-In}_2\text{Se}_3(006)$  (JCPDS 65-3639). However, based on the relative intensity listed in the JCPDS database, the contribution from  $\alpha\text{-In}_2\text{Se}_3$  is minor. Although the diffractions from higher-order peaks of the (00l) family were too weak, the result reveals that the preferred structure of  $\text{In}_x\text{Se}_y$  thin film on the GaAs(001) substrate is the defect wurtzite structure  $\gamma\text{-In}_2\text{Se}_3$ <sup>13</sup>, coexisting with the layered structure  $\alpha\text{-In}_2\text{Se}_3$ <sup>14</sup>. Once a small amount of zinc was supplied together, the layered and hexagonal structures were destroyed and the tetragonal ternary  $\text{ZnIn}_2\text{Se}_4$  dominate instead.

In brief, in-house XRD measurements reveal a rough characterization of crystallography in the whole composition range of the In-Zn-Se alloy, including the alternation of the binary structures and the formation of phase-separated and disordered compound. However, deep investigations on crystallographic characteristics were limited. The major limitation originates from the poor angular resolution of the in-house diffractometer. Because the separation of Bragg angle between  $\text{ZnSe}(h00)$  and  $\text{GaAs}(h00)$  is less than the angular resolution, these two diffraction peaks could not be completely distinguished. In order to overcome this problem, synchrotron radiation x-ray diffraction was also performed. Taking advantages of a photon flux of  $10^{10}$  photon/sec generated in BL17B and an angular resolution of 0.001 degree provided by the Huber diffractometer, not only the minor phase could be clearly identified, but also an more accurate determination of lattice parameters and corresponding built-in strain could be demonstrated for developing a model of the crystallographic transition.

As shown in Figs. 3(a) and 3(b), the radial scans along the L and H direction near the diffraction peak from GaAs(004) and GaAs(111) were plotted respectively for selected indium incorporation ratios. In this study, the L and H values are expressed in the reciprocal lattice unit (r.l.u.), which is referred to lattice constant of GaAs (JCPDS No.32-0389) with  $a=5.6538$  Å at room temperature. For the reference ZnSe thin film, based on the Bragg diffraction positions at  $L=3.9837$  and  $H=0.9976$ ,

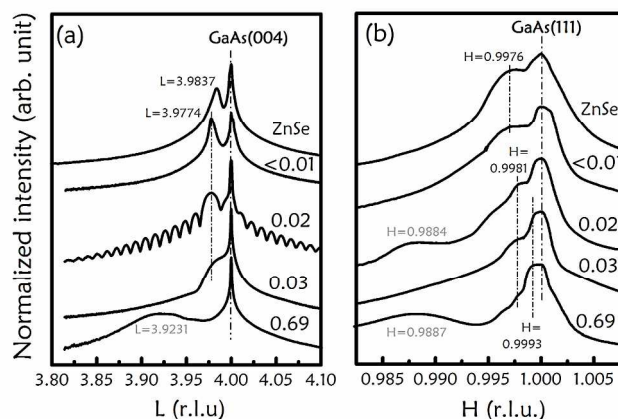


Fig. 3 Synchrotron radiation XRD spectra of (a) L-scan along GaAs(004) and (b) H-scan along GaAs(111) for specimens with selected incorporation ratio.

the surface-normal and in-plane lattice constants of 5.6769 Å and 5.6626 Å were calculated. In comparison to the relaxed value of bulk ZnSe (JCPDS No. 80-0021),  $a=5.6688$  Å, a 0.10 % in-plane contraction as well as a 0.14 % surface-normal expansion were observed, owing to the residual mismatch strain between the ZnSe film and the GaAs substrate. As for the slightly indium doped condition, in which the incorporation ratio is less than 0.01, the remained diffraction position at the H-scan together with an obvious decrease at the L-scan reveals that the in-plane and surface-normal lattice constants change to 5.6582 Å and 5.6859 Å, respectively. An increased surface-normal tension of 0.32 % was extrapolated together with an increased in-plane compression of 0.18 %. A more pronounced increasing of tension along surface normal rather than that of the in-plane compression indicates that the larger indium atoms tend to be distributed in the ZnSe lattice along the growth direction.

Once the indium solubility exceeds the detection limit to generate deficient zinc site in lattice, several tiny crystalline features, which were not detected in Fig. 2, were discovered by using synchrotron radiation apparatus. First, as the incorporation ratio of 0.02, together with the diffraction of ZnSe(111) at a higher value of  $H=0.9981$ , a much weaker peak located at  $H=0.9884$  was clearly distinguished. The new diffraction, reasonably attributed to the  $\text{ZnIn}_2\text{Se}_4(112)$  plane, indicates a small amount of phase separation in the alloy. In coincidence with the starting of zinc composition revealed by EDX measurements, it is properly to expect that the coexisting of indium incorporation and zinc lost in some unit cell which results in a defect-chalcopyrite  $\text{ZnIn}_2\text{Se}_4$  structure which contains two zinc vacancies<sup>15</sup>. On the contrary, most other unit cells remain the similar structure as the indium-doped ZnSe. In comparison to the specimen with incorporation ratio less than 0.01, the variation of tensile strain in ZnSe structure along surface normal is negligible. Nevertheless, the in-plane compression increases from 0.18 % to 0.26 %. The anisotropic feature of residual strain could also be attributed to the phase separation. We propose that because the secondary  $\text{ZnIn}_2\text{Se}_4$

structure exhibits a larger unit cell, it could provide an addition in-plane compression on the surrounding ZnSe:In structure. Owing to the small amount of ZnIn<sub>2</sub>Se<sub>4</sub>, the contribution to surface normal could be relatively small. In addition, clear interferences were observed in Fig. 3(a). According to the theory of Laue oscillation<sup>16</sup>, the relationship between the separations of the fringes  $\Delta\theta$  and the thin film thickness  $d$  is expressed as  $d = \lambda / 2 \cos \theta \Delta\theta$ , where  $\lambda$  is the wavelength of the excitation source. The extrapolated thickness is  $46 \pm 9$  nm, which coincides with the value measured by scanning electron microscopy. Moreover, because other specimens are too thick, the interference fringes were not observed.

On the contrary, the specimen with indium incorporation ratio of 0.69 also exhibits a clear phase separation while the dominant structure is ZnIn<sub>2</sub>Se<sub>4</sub> instead of ZnSe. As for the ZnIn<sub>2</sub>Se<sub>4</sub>, the L and H value of 3.9231 and 0.9887 exhibits the lattice constants of  $a = 5.6957$  Å and  $c = 11.5292$  Å. In comparison to the relaxed value, the ZnIn<sub>2</sub>Se<sub>4</sub> phase was under an in-plane contraction of 0.24 % and a surface-normal expansion of 0.70 %. On the other hand, the minor ZnSe phase exhibits a peak at  $H = 0.9993$ . Although the diffraction is too weak to be distinguished in the L-scan, a more in-plane compressive feature of ZnSe could still be expected. We proposed that the in-plane compression applied on the amount-governed ZnIn<sub>2</sub>Se<sub>4</sub> phase result from the lattice mismatch between ZnIn<sub>2</sub>Se<sub>4</sub> and GaAs, substrate. On the other hand, the increased compressive strain of the secondary ZnSe:In structure was contributed to the induced stress from the surround ZnIn<sub>2</sub>Se<sub>4</sub> matrix with larger volume of unit cell.

Finally, as for the specimen with indium incorporation ratio between 0.03 and 0.18, the synchrotron radiation measurement provides a more clear discussion on the disordered structures, which had been found by the in-house measurements. As shown in Fig. 3(b), in addition to a broad peak at the L-scan, two shoulders centred at  $H = 0.9981$  and  $H = 0.9993$  indicated that ZnSe:In structure consists of two lattice parameters. These distinguished lattice parameters coincide with the abovementioned results measured from specimens with incorporation ratio of 0.02 and 0.69. Therefore, we proposed that ZnSe:In structures are applied by two different magnitude of in-plane compression at the same time. The coexistence of different in-plane strain was proposed by the non-uniform spatial distribution of ZnIn<sub>2</sub>Se<sub>4</sub>. According to abovementioned discussions, the larger compression indicates ZnSe:In structures are surrounded by a denser amount of ZnIn<sub>2</sub>Se<sub>4</sub>. On the contrary, the smaller compression is attributed to the smaller amount of surrounded ZnIn<sub>2</sub>Se<sub>4</sub>. Therefore, the whole crystalline structure, which consists of ZnSe and ZnIn<sub>2</sub>Se<sub>4</sub>, would result in a long-range disorder. Moreover, it is interested that the disordered structure was not found at the middle range of the composition in the ternary. We suggested that the significant difference of vapour pressure between zinc and indium was a possible candidate. Because it is easier to produce zinc vacancies during the vapour-phase deposition, the starting incorporation ratio for the formation of ZnIn<sub>2</sub>Se<sub>4</sub> in the In-Zn-Se alloy of 0.02 is much lower. Owing to the synchrotron

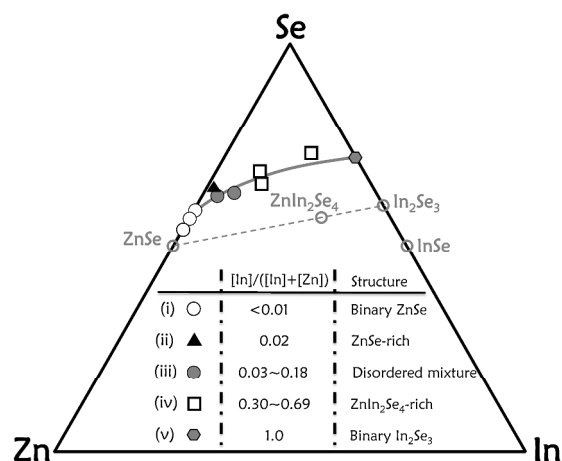
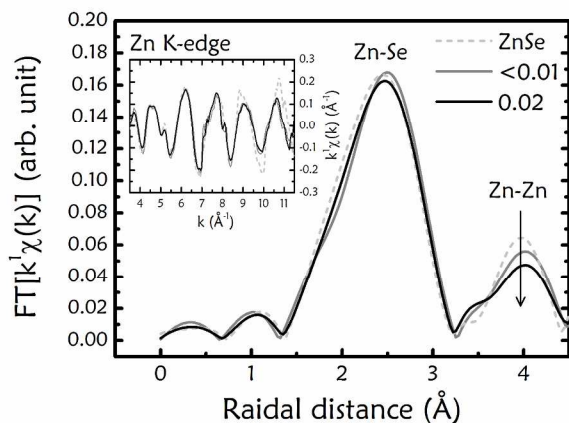


Fig. 4 Stoichiometry and crystalline of In-Zn-Se alloy plotted on the ternary phase diagram as the function of indium incorporation. The pseudo-binary tie line of ZnSe-In<sub>2</sub>Se<sub>3</sub> is also plotted.

radiation researches, the more precise prediction of phase transition was demonstrated.

In combination of stoichiometric and crystallographic results and discussions, a ternary phase diagram of In-Zn-Se alloy was established as shown in Fig. 4. The stoichiometric ZnSe, In<sub>2</sub>Se<sub>3</sub>, and ZnIn<sub>2</sub>Se<sub>4</sub> alloys, as well as the pseudo binary tie line were also plotted in the phase diagram as grey circles and the dashed line. One of the apparent features in the vapour-phase deposition is that the Se-rich stoichiometry covers the whole composition range in the In-Zn-Se alloy. Another one is that five distinct phases, including the pure ZnSe, the ZnIn<sub>2</sub>Se<sub>4</sub> embedded in a ZnSe-rich matrix, the disordered mixture, the ZnSe embedded in a ZnIn<sub>2</sub>Se<sub>4</sub>-rich matrix, and the pure In<sub>2</sub>Se<sub>3</sub>, were demonstrated and labelled as region (i) to (v), respectively. As the indium solubility increases, the separation between each phase occurs at 0.02, 0.03, 0.18, and 0.69. To our knowledge, it is the first demonstration of the specific crystallographic structures and the transition in the In-Zn-Se alloy fabricated by vapour-phase deposition.

Abovementioned discussions were based on the presumption that the large difference of vapour pressure between zinc and indium would consequentially induced zinc vacancies in the solid-state. In order to provide experimental evidence, the local atomic structure surrounding a Zn atom was investigated by evaluating the EXAFS spectra at different indium incorporation ratio. Figure 5 shows the  $k^1$ -weighted EXAFS signals and their radial distribution function after the Fourier transform (FT), where  $\gamma$  represents the magnitude of the oscillatory interference as a function of wave vector  $k$  in the range between 3.5 to 11.5 Å<sup>-1</sup>. The radial distribution function of the binary ZnSe reveals two peaks centred at 2.48 and 4.01 Å, which were attributed to the nearest Zn-Se bond and the next nearest Zn-Zn bond, respectively. The experimental results coincide with the theoretical bond lengths of zinc-blende ZnSe based on the space group F-43m. As indium atoms were doped with incorporated ratio less than 0.02, the intensity of the next



**Fig. 5** Radial distribution functions corresponding to Fourier transformed Zn K-edge EXAFS signals for specimens with selected incorporation ratio. Inset shows the origin EXAFS spectra.

nearest Zn-Zn bond gradually decreases, while that of the nearest Zn-Se bond is unchanged. One possible candidate for this difference is supported by the formation of vacancies<sup>17,18</sup>. The extrapolated coordination number of the nearest Zn-Se bond remains about 3.96 to 4.01, while that of the next nearest Zn-Zn bond decreases from 12.09 to 11.17 with the increasing indium incorporation ratio. Because the coordination numbers of a perfect ZnSe structure are 4 and 12 for the nearest and next nearest bond, the decreasing value of the Zn-Zn bond indicates the formation of zinc vacancies after indium incorporation.

## 2. Electronic structures in the In-Zn-Se alloy

Following the investigations on the crystallography, the discovery of corresponding electronic structures of each phase in the In-Zn-Se alloy was demonstrated because the material would be designed for a candidate of optoelectronics. First, to determine whether the alloy satisfies direct or indirect transition and the bandgap energy, reflectance spectra were measured at room temperature as shown in Fig. 6(a). Oscillations observed in some specimen were attributed to the interference between the thin film and the substrate. By considering the reflection from surface of thin film and the film/substrate interface, the absorption coefficient  $\alpha$  of a thin film with thickness  $t$  was extrapolated from the reflectance spectra as expressed in the following formula<sup>19</sup>,

$$2\alpha t = \ln\left(\frac{R_{\max} - R_{\min}}{R(E) - R_{\min}}\right) \quad (1)$$

where  $R(E)$  is the reflection as a function of incident photon energy  $h\nu$ ,  $R_{\max}$  and  $R_{\min}$  are the maximum and minimum value of reflection in the spectrum, respectively. Therefore, the relationship between the absorption coefficient extracted by reflectance spectra and the incident photon energy could be expressed as,

$$\alpha \propto (h\nu - E_g)^n \quad (2)$$

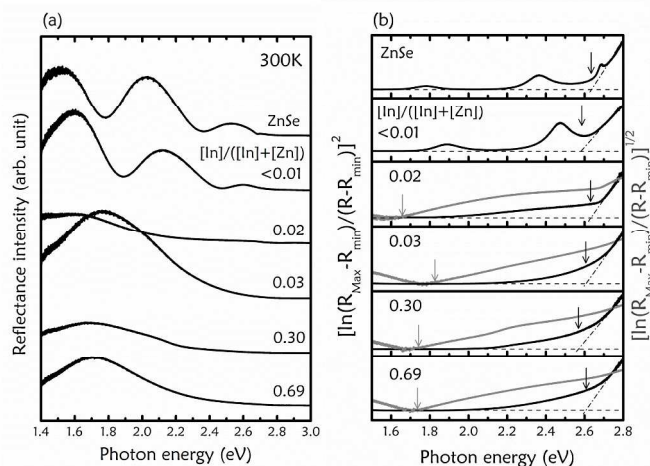


**Fig. 6** (a) Reflectance spectra measured at room temperature for specimens with selected incorporation ratio. (b) Calculated absorption coefficient based on Eq. (1) for direct (black curves) and indirect (grey curves) absorption process.

where  $n=1/2$  ( $n=2$ ) follows a direct (indirect) transition. In Fig. 6(b), the square and square root of energy dependent absorption coefficient were plotted. The linear behaviour of energy dependent absorption coefficient was found and the respective bandgap energies of direct and indirect transition were calculated according to the intercept of the x-axis.

As for the alloy with indium incorporation ratio less than 0.01, the direct interband transition dominates with bandgap energy of 2.628 eV for binary ZnSe and 2.587 eV for alloy with incorporation ratio less than 0.01. Once the supplied indium flux is large enough for hinder zinc incorporation, a secondary  $\text{ZnIn}_2\text{Se}_4$  phase occurs. In region (i) both a direct transition of 2.624 eV and an indirect transition of 1.662 eV were extrapolated and contributed to ZnSe and  $\text{ZnIn}_2\text{Se}_4$ , respectively. In comparison to the crystallographic measurements, ZnSe with major amount dominates the optical transition. As for the region (iv), the direct transition energy from ZnSe are 2.569 and 2.610 eV, and the indirect transition occurs at 1.743 and 1.734 eV for indium incorporation ratio of 0.30 and 0.69, respectively. In this region, the dominant optical transition occurs from the  $\text{ZnIn}_2\text{Se}_4$  phase instead. In particular, as for the disordered region (iii), in which the contribution from ZnSe and  $\text{ZnIn}_2\text{Se}_4$  is comparable, the determination of the electronic structure is more complicated. Moreover, absorption process out that the wide mid-gap states are more pronounced in this disordered structure. These results indicate that only the reflectance measurement is not enough for understanding the origin of optical transition. Hence the photoluminescence measurements at various temperatures were performed as shown in Fig. 7.

The binary ZnSe reference film exhibits a clear and narrow near-band-edge emission, labelled as emission A, with transition energy of 2.8 eV at 10 K as well as the negligible detection of deep level emission. The temperature-dependent peak positions of the near-band-edge emission satisfy the Varshni's description as shown in Fig. 7(b). As for the slightly

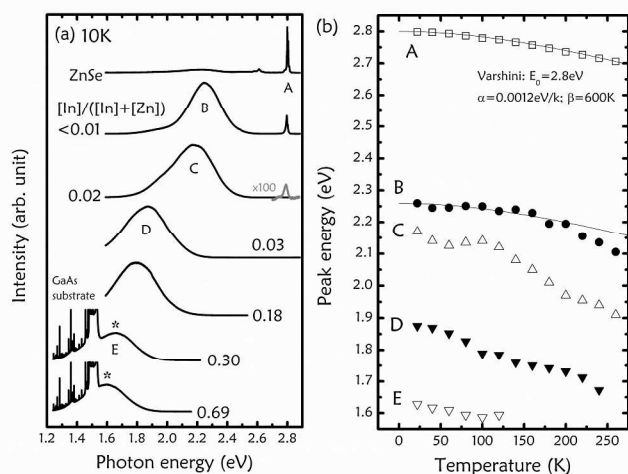


**Fig. 7** (a) Photoluminescence spectra measured at 10 K for specimens with selected incorporation ratio. (b) Dependence of peak energy on temperature for peak A to E labelled in (a). Solid lines are results of Varshini's description.

incorporation of indium in ZnSe, in which the crystallographic structure remains as pure ZnSe, an additional broad deep emission, labelled as emission B, occurs. It is obvious that the relative intensity from the near-band-edge emission is suppressed. Furthermore, once the indium incorporation ratio is large enough to generate phase separation, the near-band-edge emission of ZnSe is almost negligible. In region (ii), where ZnSe structure still dominates, the main emission centred at about 2.18 eV was labelled as emission C. Although the peak position of emission B and C at low temperature is similar and close to the theoretically predicted energy position of zinc vacancies at about 0.7 eV above the valance band maximum<sup>20</sup>, the respective temperature dependence is quite different as shown in Fig. 7(b). The temperature-dependent behaviour of emission B obeys the Varshini's prediction as the emission A whereas the behaviour of emission C exhibits a clear red-blue-red shift with the increasing temperature. The monotonic behaviour implies that emission B is originated from separated point defects of zinc vacancies. In addition, the phenomenon is similar to previously reported yellow emission for indium-doped ZnSe<sup>10</sup>. On the contrary, the red-blue-red feature of emission C, also known as the S-shape, is understood in terms of the localised carrier transition via extended states in the forbidden gap induced by high density of zinc vacancies. At a low temperature, preferred carrier recombination occurs at the shallower levels of the mid-gap states. As the temperature increases, localised carriers gain sufficient thermal energy to transport to adjacent lower levels of the states and the red-shift of luminescence takes place. The following blue-shift starting at 60 K is a result of the promoted thermal population of higher energy levels in the extended states. Finally, as the temperature exceeds 120 K, the coincidence of Varshini's prediction occurs, which indicates the delocalisation process of carriers.

As for the specimen within region (iii) where the disordered structure dominates, the main emission D of 1.9 eV at 10 K exhibits a stronger localisation effect. The temperature where

the second red-shift starts is about 200 K, indicating the localisation energy is about twice larger than that of emission C. We proposed that in the disordered mixture, the non-uniform distribution of zinc vacancies together with the phase interface between ZnSe and ZnIn<sub>2</sub>Se<sub>4</sub> would strongly destroy the whole periodic stacking of lattice, thus the spreading of mid-gap localised states are enlarged. Consequently, in combination with the reflectance and the temperature-dependent PL, it is suggested that the mid-gap localised states dominate the electronic structure in the disordered alloy.

In addition, for specimens within region (iv) where the ZnIn<sub>2</sub>Se<sub>4</sub> phase dominates, a broad emission E centred at about 1.6 eV was found in the 10 K spectrum and marked by grey star symbols in Fig. 7(a). Some sharp peaks were also observed on top of this broad peak, which was attributed to the emission from the GaAs substrate. Because of the indirect nature of ZnIn<sub>2</sub>Se<sub>4</sub> as revealed in Fig. 6, the luminescence intensity from the thin film is relatively low than that from the substrate. Moreover, the localisation effect is not apparent within region (iv). The author suggested that because the zinc vacancy is a crucial part for creating the defect-chalcopyrite ZnIn<sub>2</sub>Se<sub>4</sub> structure<sup>15</sup>, the probability of alteration to the periodic ordering and the resultant mid-gap states is weaker.

Based on the EXAFS and optical investigations, it could be summarised that zinc vacancies distributed in ZnSe-based structure behave more opportunities to alter the zinc-blende lattice. The highest density of localised states occurs in region (iii) where the global structure is disordered, and dominates the optical transition. In general, such a high density of mid-gap states would promote carrier occupation and lower the Fermi level position as reported in the AlGaIn thin film<sup>21</sup>. In order to confirm this assumption, the energy difference between Fermi level and the top of valance band was extrapolated by the x-ray photoelectron spectroscopy as shown in Fig. 8 for selected specimens within region (i), (ii), (iii), and (iv), with a magnified inset figure which reveals the low binding energy portion. The

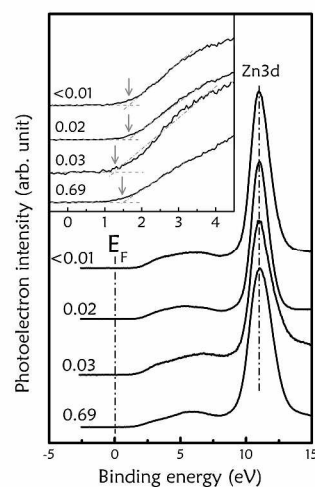


**Fig. 8** X-ray photoelectron spectroscopy spectra measured near valance band for specimens with selected incorporation ratio. The inset shows the magnified curves with low binding energy.

binding energy in this measurement was calibrated by using the core level emission from Zn 3d subshell of 11 eV<sup>22</sup>. The energy position of the Fermi level and the valance band maximum were determined at the zero-energy point and the linear intercept of the steep inclining from the base line, respectively. As shown in the inset figure, the energy difference between the Fermi level and the valance band maximum decreases from 1.79 eV for region (i) to 1.41 eV for region (iii). Such a 0.38 eV reduction of the Fermi level position indicates the significantly increased density of localised state. In summary, the EXAFS, the temperature dependent PL, and the XPS results provided that heavily indium incorporation would cause zinc vacancies in the alloy, which act as the self-compensating centres in previous literatures<sup>9-11</sup>.

Furthermore, special characteristics of the disordered mixture in the In-Zn-Se alloy were pointed out for the indium incorporation ratio between 0.03 and 0.18 in this work. The nature of amorphous-like structure shows advantages on fabrication processes. For instance, the limit of substrate could possibly be overcome in the future. In particular, the light absorption occurs widely in the visible range. Based on these features, disordered In-Zn-Se alloy would be expected as a potential candidate for intermediate-band optoelectronic devices.

## Conclusions

In conclusion, the transition of fundamental characteristics including the stoichiometry, the crystallography and the electronic structures of the MBE-grown In-Zn-Se alloy was demonstrated. During the vapour phase deposition, the large difference of vapour pressure between indium and zinc results in deficient Zn in solid state. Once the indium incorporation is large enough, the phase-separated alloy consists of the ZnSe structure with Zn vacancy and the defect-chalcopyrite ZnIn<sub>2</sub>Se<sub>4</sub> structure is generated. The competition of these two phases results in the crystallographic transition which starts from the pure ZnSe and is followed by the ZnSe-rich, the amorphous-like mixture, the ZnIn<sub>2</sub>Se<sub>4</sub>-rich, and the pure In<sub>2</sub>Se<sub>3</sub> in sequence. The separation between each phase and the corresponding strain were also determined by using the synchrotron radiation apparatus. In particular, the disordered mixture occurs as the indium incorporation ratio range from 0.03 to 0.18, in which the amount of the two phases is compatible. In this condition, wide-distributed localised states induced by high density of zinc vacancies are observed in the forbidden gap. These results herein provide effective feasibilities for applying the II-III<sub>2</sub>-IV<sub>4</sub> alloy to the next generation optoelectronics devices.

## Acknowledgements

This work was supported by the National Science Council under grant No. NSC 100-2221-E-036-015. The authors would like to thank Precious Instrument Center of National Chiao Tung University for providing EDX instruments.

## Notes and references

<sup>a</sup> Center of Nanoscience and Technology, Tunghai University, Taichung, Taiwan, Republic of China. E-mail: leeling@thu.edu.tw

<sup>b</sup> Graduated Institute of Electro-Optical Engineering, Tatung University, Taipei, Taiwan, Republic of China. E-mail: csyang@ttu.edu.tw

<sup>c</sup> National Synchrotron Radiation Research Center, Hsinchu, Tainan 701, Taiwan, Republic of China

- 1 P. Jackson, D. Hariskos, E. Lotter, S. Paetel, R. Wuerz, R. Manner, W. Wischmann, and M. Powalla, *Prog. Photovoltaics*, 2011, **19**, 894.
- 2 S. H. You, K. J. Hong, T. S. Jeong, and C. J. Youn, *J. Appl. Phys.*, 2009, **106**, 043518.
- 3 V. M. Nikale, S. S. Shinde, A. R. Babar, C. H. Bhosale, and K. Y. Rajpure, *Solar Energy*, 2011, **85**, 1336.
- 4 K.-W. Cheng, Y.-H. Cheng, and M.-S. Fan, *Int. J. Hydro. Energy*, 2012, **37**, 13763.
- 5 S. P. Yadav, P. S. Shinde, K. Y. Rajpure, and C. H. Bhosale, *Solar Energ. Mater. Solar Cells*, 2008, **92**, 453.
- 6 Y. Ohtake, S. Chaisitsak, A. Yamada, and M. Konagai, *Jpn. J. Appl. Phys.*, 1998, **37**, 3220.
- 7 S.-H. Choe, *Curr. Appl. Phys.*, 2009, **9**, 1.
- 8 R. Jeyakumar, S. T. Lakshmikummar, and A. C. Rastogi, *Mater. Res. Bull.*, 2002, **37**, 617.
- 9 B. R. Sethi, and P. C. Mathus, *Phys. Stat. Sol. (a)*, 1978, **46**, 717.
- 10 A. N. Georgobiani, U. A. Aminov, Yu. V. Korostelin, V. I. Kozlovsky, A. S. Nasibov, and P. V. Shapkin, *J. Cryst. Growth*, 1998, **184**, 470.
- 11 P. V. Shapkin, A. S. Nasibov, Yu. F. Vaksman, Yu. A. Nitsuk, and Yu. N. Purtov, *Inorg. Mater.*, 2006, **42**, 845.
- 12 R. E. Honig, and D. A. Kramer, *RCA Review*, 1969, **30**, 285.
- 13 A. Likoforman, D. Carre, and R. Hillel, *Acta Crystallogr. Sec. B: Struct. Crtsrallogr. Cryst. Chem.*, 1978, **34**, 1.
- 14 S. Popovic, A. Tonejc, B. Grzeta-Plenkovic, B. Celustka, and R. Trojko, *J. Appl. Crystallogr.*, 1979, **12**, 416.
- 15 M. Ishikawa, and T. Nakayama, *J. Cryst. Growth*, 2000, **214**, 452.
- 16 B. Warren, in *X-ray Diffractions*, Dover, New York, 1990.
- 17 S. J. A. Figueroa, F. G. Requejo, E. J. Lede, L. Lamaita, M. A. Peluso, and J. E. Sambeth, *Catalysis Today*, 2005, **107**, 849.
- 18 K. Ahn, D. S. Yoo, D. H. Prasad, H.-W. Lee, Y.-C. Chung, and J.-H. Lee, *Chem. Mater.*, 2012, **24**, 4261.
- 19 V. Kumar, S. Kr. Sharma, T. P. Sharma, and V. Singh, *Opt. Mater.*, 1999, **12**, 115.
- 20 B. K. Meyer, and W. Stadler, *J. Cryst. Growth*, 1996, **161**, 119.
- 21 C. S. Ku, K. M. Peng, W. C. Ke, H. Y. Huang, N. E. Tang, W. K. Chen, W. H. Chen, and M. C. Lee, *Appl. Phys. Lett.*, 2004, **85**, 2818.
- 22 C.-S. Lee, L. Larina, Y.-M. Shin, E. A. Al-Ammar, and B. T. Ahn, *Phys. Chem. Chem. Phys.*, 2012, **14**, 4789.

## Table of contents entry

Transition of crystallographic and electronic structures in In-Zn-Se alloys grown by molecular beam epitaxy

### Synopsis:

Owing to zinc vacancies induced during the vapour-phase deposition, the stoichiometric and crystallographic evolutions in the In-Zn-Se alloy, five distinguished phases, and the corresponding electronics structures were demonstrated.

